Few-shot Non-line-of-sight Imaging with
Signal-surface Collaborative Regularization (Supplement)

Xintong Liu[1], Jianyu Wang[1], Leping Xiao[1], Xing Fu[1], Lingyun Qiu[1,2], and Zuoqiang Shi[1,2]
[1]Tsinghua University
[2]Yanqi Lake Beijing Institute of Mathematical Sciences and Applications

1. Introduction

- In section 2 we discuss the solution of the proposed SSCR algorithm in detail. We also show that the parameters in the algorithm can be chosen adaptively. The time and memory complexity of each sub-problem is analyzed and comparisons with existing reconstruction algorithms are provided.

- In section 3 we show additional reconstruction results of the statue without using regularizations. See also Fig. 2 and Fig. 3 in the main article.

- In section 4 we show additional reconstruction results of the pyramid. See also Fig. 4 in the main article.

- In section 5 we show additional reconstruction results of the statue. See also Fig. 5 and Fig. 6 in the main article.

2. The SSCR algorithm

The optimization problem of the proposed signal-surface collaborative regularization (SSCR) method writes

$$
\begin{aligned}
\arg\min_{\substack{\boldsymbol{\tau},\mathbf{u},\mathbf{g},\\ D_s,D_n,\mathbf{C},S}} & \sum_{p,q}[(d_{p,q}-N)\ln(1-\tau_{p,q})-d_{p,q}\ln(\tau_{p,q})]\\
& + \lambda_t\|\mathcal{P}(\boldsymbol{\tau})-DS\|_2^2 + \lambda_{ut}\|\mathcal{P}(A\mathbf{u})-DS\|_2^2 + \lambda_{pt}|S|_0\\
& + \lambda\|\boldsymbol{\tau}-A\mathbf{u}\|_2^2 + s_u\|\mathbf{u}\|_1 + \lambda_g\left[\|\mathbf{u}-\mathbf{g}\|_2^2+\Upsilon(\mathbf{g})\right]\\
& + \lambda_u\sum_i\left[\|\mathcal{B}\mathbf{u}_i-D_sC_iD_n^T\|_2^2 + \lambda_{pu}|C_i|_0\right]\\
s.t. \ \ & \mathbf{g}\in\mathcal{G}, \ \ D_sD_s^T=I_x, \ \ D_nD_n^T=I_y,
\end{aligned}
$$
(S1)

in which p and q are the indices of the measurement pair and the time bin, respectively. N is the number of pulses used for each measurement pair. $d_{p,q}$ is the number of the photon events recorded. The optimization problem contains several parameters, namely, λ_t, λ_{ut}, λ_{pt}, λ, s_u, λ_g, λ_u and λ_{pu}. We discuss the solutions to the sub-problems of the

---

Algorithm S1 Solving the sub-problem (S4)

Require: $\boldsymbol{\tau}^0$, s_u^{imp}, μ_s.
Ensure: $\mathbf{u}^0$.
  $\mathbf{b}_0^0 = \mathbf{0}$
  $\mathbf{u}_0^0 = \arg\min_{\mathbf{u}}\|A\mathbf{u}-\boldsymbol{\tau}^0\|_2^2$
  for $j=0$ to $J-1$ **do**
    $\mathbf{v}_{j+1}^0 = \arg\min_{\mathbf{v}} s_u^{\text{imp}}\|\mathbf{v}\|_1 + \mu_s\left\|\mathbf{v}-\mathbf{u}_j^0+\mathbf{b}_j^0\right\|_2^2$
    $\mathbf{u}_{j+1}^0 = \arg\min_{\mathbf{u}}\|A\mathbf{u}-\boldsymbol{\tau}^0\|_2^2 + \mu_s\left\|\mathbf{v}_{j+1}^0-\mathbf{u}+\mathbf{b}_j^0\right\|_2^2$
    $\mathbf{b}_{j+1}^0 = \mathbf{b}_j^0 + \mathbf{v}_{j+1}^0 - \mathbf{u}_{j+1}^0$
  end for
  $\mathbf{u}^0 = \mathbf{v}_J^0$

---

proposed SSCR algorithm (See Algorithm 1 in the main article) step by step. We assume that the reconstruction domain is discretized with $L\times L\times L$ voxels and $p=\mathcal{O}(1)$, $q=\mathcal{O}(L)$ for few-shot NLOS imaging scenarios.

2.1. The initialization stage

(A1) Initializing $\boldsymbol{\tau}$ The estimated signal $\boldsymbol{\tau}$ is initialized by minimizing the data-fidelity term without regularization

$$
\tau_{p,q}^0 = \arg\min_{\tau_{p,q}}(d_{p,q}-N)\ln(1-\tau_{p,q})-d_{p,q}\ln(\tau_{p,q}), \ \ (S2)
$$

which yields a closed form solution $\tau_{p,q}^0 = d_{p,q}/N$. The time and memory complexity of this step is $\mathcal{O}(L)$.

(A2) Initializing $\mathbf{u}$ We initialize $\mathbf{u}$ by solving the following L_1 regularized problem

$$
\mathbf{u}^0 = \arg\min_{\mathbf{u}}\lambda\|\boldsymbol{\tau}^0-A\mathbf{u}\|_2^2 + s_u\|\mathbf{u}\|_1, \ \ (S3)
$$

in which λ and s_u are fixed parameters to be determined. By defining $s_u^{\text{imp}}=s_u/\lambda$, this problem is equivalent to the following optimization problem

$$
\mathbf{u}^0 = \arg\min_{\mathbf{u}}\|\boldsymbol{\tau}^0-A\mathbf{u}\|_2^2 + s_u^{\text{imp}}\|\mathbf{u}\|_1. \ \ (S4)
$$

We determine the parameter s_u^{imp} adaptively as follows. Let $\mathbf{u}^{\text{BP}} = A^T\boldsymbol{\tau}^0$ be the solution of the back-projection

Method	Confocal	Non-confocal	Reconstruction quality	Time Complexity	Memory Complexity
LOG-BP [3]	✓	✓	Frobbly	$\mathcal{O}(L^3)$	$\mathcal{O}(L^3)$
F-K [4]	✓	✗	Frobbly	$\mathcal{O}(L^3 \log L)$	$\mathcal{O}(L^3)$
PF [5]	✓	✓	Low	$\mathcal{O}(L^3 \log L)$	$\mathcal{O}(L^3)$
LCT [8]	✓	✗	Low	$\mathcal{O}(L^3 \log L)$	$\mathcal{O}(L^3)$
D-LCT [9]	✓	✗	Low	$\mathcal{O}(L^3 \log L)$	$\mathcal{O}(L^3)$
SOCR [6]	✓	✓	Medium	$\mathcal{O}(L^3)$	$\mathcal{O}(L^3)$
SSCR	✓	✓	High	$\mathcal{O}(L^3)$	$\mathcal{O}(L^3)$

Table 1. Comparisons of different NLOS imaging methods with $\mathcal{O}(1)$ measurement pairs. The proposed SSCR method provides high-quality reconstructions and enjoys low complexity.

(BP) algorithm. We use the conjugate gradient method to solve the least-squares problem $\min_{\mathbf{u}} \|\boldsymbol{\tau}^0 - A\mathbf{u}\|_2^2$ with initial guess $\mathbf{u}^{\text{BP}}$. The maximum number of iterations is set to be 20, and the iteration breaks whenever the relative residual of the linear system $A^T A \mathbf{u} = A^T \boldsymbol{\tau}^0$ reaches below 0.5%. The output is denoted by $\mathbf{u}^{\text{LS}}$. The parameter s_u^{imp} is determined as

$$s_u^{\text{imp}} = k_{\text{sparse}} \frac{\|\boldsymbol{\tau}^0 - A\mathbf{u}^{\text{LS}}\|_2^2}{\|\mathbf{u}^{\text{LS}}\|_1}, \tag{S5}$$

where $k_{\text{sparse}} = 10$ by default. This problem can be solved efficiently using the split Bregman method [2]. The main steps are shown in Algorithm S1.

To carry out the iteration process, a new parameter μ_s is introduced. Empirically, we set this parameter as

$$\mu_s = \frac{\|\mathbf{u}\|_0}{2\|\mathbf{u}\|_1} s_u^{\text{imp}}. \tag{S6}$$

In each iteration, the variable $\mathbf{v}$ can be updated using the soft-thresholding operator [2]. To update the variable $\mathbf{u}$, the conjugate gradient method is applied, which takes $\mathcal{O}(L^3)$ memory and computational cost.

2.2. The iteration stage

(B1) Updating g The variable $\mathbf{g}$ is updated as follows

$$\mathbf{g}^{k+1} = \arg\min_{\mathbf{g}} \|\mathbf{u}^k - \mathbf{g}\|_2^2 + \Upsilon(\mathbf{g}) = \mathcal{S}(\mathbf{u}^k). \tag{S7}$$

To realize the surfaciation operator $\mathcal{S}$, it suffices to solve the optimization problems (15), (17), and (19) in the main article, as listed below

- Equation (15) in the main article

$$
\begin{aligned}
\mathbf{e}^* &= (e_{ij}^*)_{I \times J} \\
&= \arg\min_{\{e_{ij}\}} \sum_{i=1}^{I} \sum_{j=1}^{J} \gamma_{ij}(e_{ij} - \tilde{e}_{ij})^2 \\
&\quad + \sum_{p=1}^{I} \sum_{q=1}^{J} \sum_{r=1}^{I} \sum_{s=1}^{J} w_{pq,rs}^{\mathbf{e}}(e_{pq} - e_{rs})^2.
\end{aligned}
\tag{S8}
$$

- Equation (17) in the main article

$$
\begin{aligned}
\mathbf{d}^* &= (d_{ij}^*)_{I \times J} \\
&= \arg\min_{\{d_{ij}\}} \sum_{i=1}^{I} \sum_{j=1}^{J} \sum_{n=1}^{n_{ij}} \lambda_{ijn}(d_{ij} - z_{k_{ij}^n})^2 \\
&\quad + \sum_{p=1}^{I} \sum_{q=1}^{J} \sum_{r=1}^{I} \sum_{s=1}^{J} w_{pq,rs}^{\mathbf{d}}(d_{pq} - d_{rs})^2.
\end{aligned}
\tag{S9}
$$

- Optimization problem (19) in the main article

$$
\begin{aligned}
\min_{\{\alpha_{ij}\}} &\sum_{i=1}^{I} \sum_{j=1}^{J} \sum_{n=1}^{n_{ij}} \lambda_{ijn}(\alpha_{ij} - u_{ijk_{ij}^n})^2 \\
&+ \sum_{p=1}^{I} \sum_{q=1}^{J} \sum_{r=1}^{I} \sum_{s=1}^{J} w_{pq,rs}^{\boldsymbol{\alpha}}(\alpha_{pq} - \alpha_{rs})^2.
\end{aligned}
\tag{S10}
$$

Noting that

$$\sum_{n=1}^{n_{ij}} \lambda_{ijn}(d_{ij} - z_{k_{ij}^n})^2 = \lambda_{ij}\left(d_{ij} - \sum_{n=1}^{n_{ij}} r_{ijn} z_{k_{ij}^n}\right)^2, \tag{S11}$$

and

$$\sum_{n=1}^{n_{ij}} \lambda_{ijn}(\alpha_{ij} - u_{ijk_{ij}^n})^2 = \lambda_{ij}\left(\alpha_{ij} - \sum_{n=1}^{n_{ij}} r_{ijn} u_{k_{ij}^n}\right)^2, \tag{S12}$$

2

in which $u_{k_{ij}^n} = u_{ijk_{ij}^n}$, $\lambda_{ij} = \sum_{n=1}^{n_{ij}} \lambda_{ijn}$ and $r_{ijn} = \lambda_{ijn}/\lambda_{ij}$, it suffices to solve the problem of the following type

$$F(\mathbf{u}; \boldsymbol{\lambda}, \mathbf{w}) = \sum_i \lambda_i (u_i - d_i)^2 + \sum_{ij} w_{ij}(u_i - u_j)^2, \quad \text{(S13)}$$

in which $\mathbf{u}$ is the optimization variable, $\boldsymbol{\lambda}$ and $\mathbf{w}$ are fixed weights. The solution to this least-squares problem can be obtained by solving the linear system

$$\lambda_i u_i + \sum_{k \neq i}(w_{ik} + w_{ki})u_i - \sum_{k \neq i}(w_{ik} + w_{ki})u_k = \lambda_i d_i,$$
$$\text{(S14)}$$

for all i. We use the widely acknowledged LSQR method to solve this problem. For the parameters $w_{pq,rs}^{\mathbf{e}}$, $w_{pq,rs}^{\mathbf{d}}$ and $w_{pq,rs}^{\boldsymbol{\alpha}}$, we set $w_{pq,rs}^{\mathbf{e}} = w_{pq,rs}^{\mathbf{d}} = w_{pq,rs}^{\boldsymbol{\alpha}} = w_{pq,rs}$ and define

$$w_{pq,rs} = \begin{cases} 1, & \max\{|p-r|, |q-s|\} = 1 \\ 0, & \text{otherwise} \end{cases} \quad \text{(S15)}$$

In the main article, we have provided basic introductions for the determinations of $\mathbf{e}^*$, $\mathbf{d}^*$, and $\boldsymbol{\alpha}$. For high noise-robustness, the parameters γ_{ij}, λ_{ijn} and data $\tilde{e}_{ij}$ are related with the input $\mathbf{u}$. We show all steps in detail, which matches the supplementary code.

- Step 1: Determining $\mathbf{d}^*$ with $\mathbf{u}$. Set $\lambda_{ij} = 2$, $r_{ijn} = 2u_{ijn}^2 / \sum_{n=1}^{n_{ij}} u_{i,j,k_{ij}^n}^2$. For simplicity, in Eq. (S9) we replace $z_{k_{ij}^n}$ in the data fidelity term with k_{ij} for the implementation of the code. We obtain the solution of (S9) with Eq. (S11).

- Step 2: Determining $\boldsymbol{\alpha}$ with $\mathbf{u}$ and $\mathbf{d}^*$. Set $\lambda_{ij} = 1$ and $r_{ijn} = r'_{ijn} / \sum_{n=1}^{n_{ij}} r'_{ijn}$ with

$$r'_{ijn} = \begin{cases} (d_{ij}^* - k_{ijn})^{-2}, & d_{ij}^* \neq k_{ijn} \\ 2, & \text{otherwise} \end{cases}, \quad \text{(S16)}$$

in which d_{ij}^* is obtained in Step 1. We obtain the solution of (S10) with Eq. (S12).

- Step 3: Determining $\mathbf{e}^*$ with Eq. (S8). Let α_{max}^* be the maximum value of $\boldsymbol{\alpha}^*$. The parameter γ_{ij} is set as $\gamma_{ij} = \alpha_{ij}^* / (2\alpha_{max}^*)$. Besides, we reset γ_{ij} to be 0.75 if (i, j) is a background pixel of $\mathbf{u}$ or

$$\sum_{n=1}^{n_{ij}} r_{ijn} u_{k_{ij}^n} < 0.1 u_{max}^{\text{inter}}, \quad \text{(S17)}$$

in which r_{ijn} is defined in Step 2 and $u_{max}^{\text{inter}} = \max_{i,j}\{\sum_{n=1}^{n_{ij}} r_{ijn} u_{k_{ij}^n}\}$. In the main article, we choose the data $\tilde{e}_{ij}$ to be the indicator function of the foreground pixels for simplicity. For high noise-robustness, we set $\tilde{e}_{ij} = (\sum_{n=1}^{n_{ij}} r_{ijn} u_{k_{ij}^n})/u_{max}^{\text{inter}}$ for

foreground pixels (i, j) of $\mathbf{u}$ and 0 for background pixels (i, j) of $\mathbf{u}$. The solution of Eq. (S8) is used to determine the foreground set of $\mathbf{g}$ by comparing the values with 0.5, as discussed in Eq. (15) of the main article.

Noting that we use sparse weights in the least-squares problems, the time and memory complexity of this step is $\mathcal{O}(L^3)$.

(B2) Updating the triplet $(D_s, \mathbf{C}, D_n)$ The orthogonal matrices D_s and D_n capture the local structures and non-local correlations of the reconstruction $\mathbf{u}$, respectively. The tensor $\mathbf{C}$ consists of the sparse transform coefficients of the block dataset of the albedo values. The triplet $(D_s, \mathbf{C}, D_n)$ is updated by solving the following optimization problem

$$(D_s^{k+1}, \mathbf{C}^{k+1}, D_n^{k+1}) = \underset{D_s, \mathbf{C}, D_n}{\arg\min} \|\mathcal{B}\mathbf{u}_i^k - D_s C_i D_n^T\|_2^2$$
$$+ \lambda_{pu}|C_i|_0, \quad \text{(S18)}$$

whose solution has been studied in the work [1,6]. The parameter λ_{pu} is chosen adaptively and implicitly by directly following the supplement of [6]. When the sizes of the local patches and searching window are $\mathcal{O}(1)$, the resulting time and memory complexity is $\mathcal{O}(L^3)$. More details can be found in [6].

(B3) Updating S The matrix S contains the sparse frequency-domain coefficients of a combination of the estimated and the simulated signal. We update S by solving

$$S^{k+1} = \underset{S}{\arg\min} \lambda_t \|\mathcal{P}(\boldsymbol{\tau}^k) - DS\|_2^2$$
$$+ \lambda_{ut}\|\mathcal{P}(A\mathbf{u}^k) - DS\|_2^2 + \lambda_{pt}|S|_0. \quad \text{(S19)}$$

By setting $\lambda_{ut}^{\text{imp}} = \lambda_{ut}/\lambda_t$ and $\lambda_{pt}^{\text{imp}} = \lambda_{pt}/\lambda_t$, this problem is equivalent to the following optimization problem.

$$S^{k+1} = \underset{S}{\arg\min} \|\mathcal{P}(\boldsymbol{\tau}^k) - DS\|_2^2$$
$$+ \lambda_{ut}^{\text{imp}}\|\mathcal{P}(A\mathbf{u}^k) - DS\|_2^2 + \lambda_{pt}^{\text{imp}}|S|_0. \quad \text{(S20)}$$

We set $\lambda_{ut}^{\text{imp}} = 1$. Interested readers are referred to equation (S.7) in the supplement of [7] for the solution to this problem and the implicit choices of $\lambda_{pt}^{\text{imp}}$. When the patch sizes of the signal are $\mathcal{O}(1)$, the time and memory complexity of this step is $\mathcal{O}(L)$.

(B4) Updating $\boldsymbol{\tau}$ The estimated signal $\boldsymbol{\tau}$ is updated with

$$\boldsymbol{\tau}^{k+1} = \underset{\boldsymbol{\tau}}{\arg\min}$$
$$\sum_{p,q}[(d_{p,q} - N)\ln(1 - \tau_{p,q}) - d_{p,q}\ln(\tau_{p,q})]$$
$$+ \lambda_t\|\mathcal{P}(\boldsymbol{\tau}) - DS^{k+1}\|_2^2 + \lambda\|\boldsymbol{\tau} - A\mathbf{u}^k\|_2^2, \quad \text{(S21)}$$

3

in which $\mathcal{P}$ is the patch generating operator. Let $\mathcal{P}^*$ be the patch aggregation operator that maps the patch dataset back to the signal, such that $\mathcal{P}^* \circ \mathcal{P}$ is the identity transform. We assume that

$$\lambda_t \|\mathcal{P}(\boldsymbol{\tau}) - DS^{k+1}\|_2^2 = \bar{\lambda}_t \|\boldsymbol{\tau} - \mathcal{P}^*(DS^{k+1})\|_2^2. \quad \text{(S22)}$$

This equation holds precisely using the boundary extension and zero padding techniques. It suffices to determine the parameter $\bar{\lambda}_t$. In the following, we abuse the notation and write $\bar{\lambda}_t$ as λ_t for simplicity. With this treatment, the objective function of Eq. (S21) can be rewritten as

$$\sum_{p,q} [(d_{p,q} - N) \ln(1 - \tau_{p,q}) - d_{p,q} \ln(\tau_{p,q})]$$
$$+ (\lambda_t + \lambda) \left\| \boldsymbol{\tau} - \frac{\lambda_t \mathcal{P}^*(DS^{k+1}) + \lambda A \mathbf{u}^k}{\lambda_t + \lambda} \right\|_2^2. \quad \text{(S23)}$$

In this problem, we set the parameters λ_t and λ implicitly as

$$\lambda_t = \lambda = \frac{\sum_{p,q}[(d_{p,q} - N) \ln(1 - \tau_{p,q}^0) - d_{p,q} \ln(\tau_{p,q}^0)]}{\left\| \boldsymbol{\tau}^0 - \frac{1}{2}(\mathcal{P}^*(DS^1) + A\mathbf{u}^0) \right\|_2^2} \quad \text{(S24)}$$

Noting that the variables $\{\tau_{p,q}\}$ are decoupled, it suffices to solve the problem of the following type

$$\min_{\tau} \ f(\tau) = (d-N) \ln(1-\tau) - d \ln(\tau) + \mu(\tau-s)^2, \quad \text{(S25)}$$

in which N is a positive integer, $d \in [0, N]$ is a positive integer. $\mu > 0$ and s are fixed parameters. We find τ in the interval $[0, 1]$. This is a convex optimization problem, and the situation breaks down into three cases depending on the value of d.

- Case 1: $d = 0$. The term $-d \ln(\tau)$ vanishes and a change of variable $s^* = 1 - s$ converts this situation to Case 3. The solution is given by

$$\tau_{opt} = \max \left\{ 0, 1 - \frac{1}{2} \left(1 - s + \sqrt{(1-s)^2 + \frac{2N}{\mu}} \right) \right\}. \quad \text{(S26)}$$

- Case 2: $0 < d < N$. The objective function is strictly convex in the interval $(0, 1)$ with $f(0+) = f(1-) = +\infty$. Differentiating with respect to τ, we deduce that the solution is the unique real zero point of the cubic polynomial

$$p(x) = x^3 - (s+1)x^2 + (s - \frac{N}{2\mu})x + \frac{d}{2\mu} \quad \text{(S27)}$$

in the interval $(0, 1)$.

- Case 3: $d = N$. This never happens in real-world experiments. In this case, the term $(d - N) \ln(1 - \tau) - d \ln(\tau)$ vanishes and the closed-form solution is given by

$$\tau_{opt} = \min \left\{ 1, \frac{1}{2} \left(s + \sqrt{s^2 + \frac{2N}{\mu}} \right) \right\}. \quad \text{(S28)}$$

For the cases 1 and 3, it takes $\mathcal{O}(1)$ to compute τ_{opt}. For the case 2, it suffices to compute and filter the eigenvalues of the companion matrix of the cubic polynomial (S27), which also takes $\mathcal{O}(1)$. Thus, the overall time and memory complexity of this step is $\mathcal{O}(L^3)$. Other tricks to determine the foreground indication matrix $\mathbf{e}$ are provided in the supplementary code.

(B5) Updating u The reconstructed target is updated with

$$\begin{aligned}
\mathbf{u}^{k+1} = \arg \min_{\mathbf{u}} & \ \lambda \|\boldsymbol{\tau}^{k+1} - A\mathbf{u}\|_2^2 + \lambda s_u \|\mathbf{u}\|_1 \\
& + \lambda_{ut} \|\mathcal{P}(A\mathbf{u}) - DS^{k+1}\|_2^2 \\
& + \lambda_u \sum_i \|\mathcal{B}\mathbf{u}_i - D_s^{k+1} C_i^{k+1} (D_n^{k+1})^T\|_2^2 \\
& + \lambda_g \|\mathbf{u} - \mathbf{g}^{k+1}\|_2^2.
\end{aligned} \quad \text{(S29)}$$

We refer to equation (S.9) and Algorithm 4 in the supplement of [6] for the solution to this problem and corresponding choices of the parameters λ_{ut}, λ_u. The method of choosing λ_g implicitly is completely analogous to that of λ_{ut}. Similar to step (A2), the time and memory complexity of this step is $\mathcal{O}(L^3)$.

The overall time and memory complexity of the proposed method is $\mathcal{O}(L^3)$ when $P = \mathcal{O}(1)$. Comparisons of the proposed SSCR algorithm with existing methods are shown in Table 1.

3. Reconstructions without regularizations

In Fig. 2 and Fig. 3 of the main article, we present the least-squares solution and the corresponding simulated signal for the instance of the statue with 3×3 confocal measurements. The coordinates of the focal points are provided in the supplementary code. The original measured signal is provided in the work [4]. The exposure time is 60 min for the original 512×512 measurements. The time resolution is 32 ps. The voxel size is $3.17 \times 3.17 \times 0.96$ cm^3 in the horizontal, vertical and depth directions. The target is 1 m away from the visible surface. The size of the reconstruction domain is $2 \times 2 \times 0.4$ m^3 in the horizontal, vertical and depth directions. The least-squares problem without regularization writes

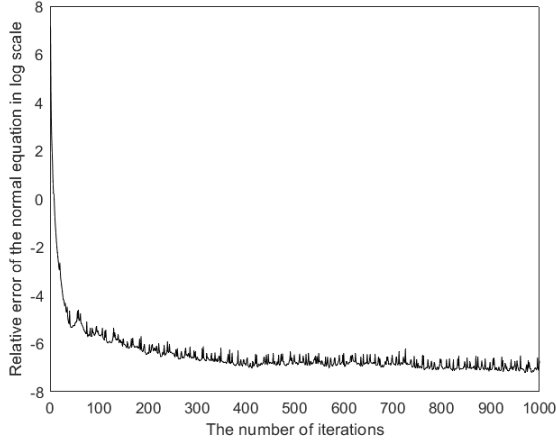$$\arg \min_{\mathbf{u}} \|A\mathbf{u} - \boldsymbol{\tau}\|_2^2, \quad \text{(S30)}$$

4

Figure S1. The relative L_2 error of the normal equation in log scale. After 1000 iterations, the relative error decreases to 0.12%.
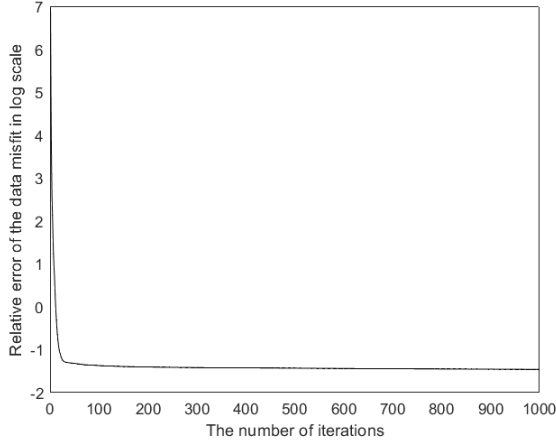

Figure S2. The relative L_2 data misfit of each iteration. The relative data misfit decreases to 23.26% after 1000 iterations.

in which A is the measurement matrix and $\boldsymbol{\tau}$ is the measured data. The solution is not unique due to the rank deficiency of A. We use the conjugate gradient method to solve the corresponding normal equation

$$A^T A \mathbf{u} = A^T \boldsymbol{\tau}. \tag{S31}$$

The initial value of $\mathbf{u}$ is set as $A^T \boldsymbol{\tau}$, which is the solution of the back-projection algorithm. The L_2 relative errors of the normal equation and the data misfit in log scales $\ln(\|A^T A \mathbf{u} - A^T \boldsymbol{\tau}\|_2 / \|A^T \boldsymbol{\tau}\|_2)$ and $\ln(\|A\mathbf{u} - \boldsymbol{\tau}\|_2 / \|\boldsymbol{\tau}\|_2)$ of the first 1000 iterations are shown in Fig. S1 and Fig. S2. The algorithm converges and the relative L_2 data misfit of the least-squares solution is 23.36%, which results from the approximation error of the physical model and measurement noise. The reconstruction results of the BP algorithm
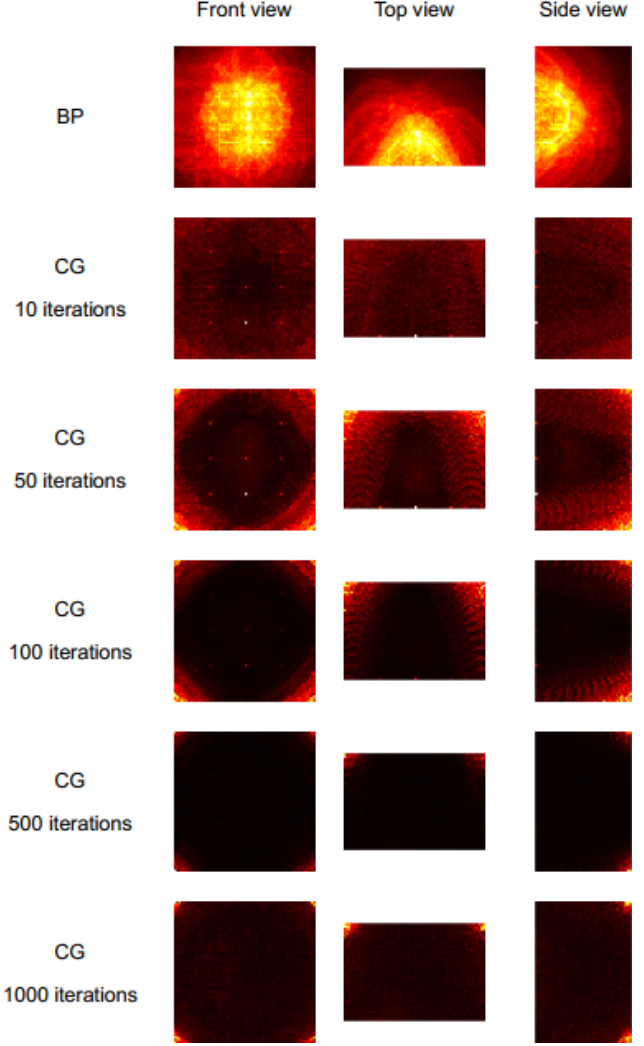
Figure S3. Reconstruction results of the statue with the back-projection algorithm and CG iterations. The target cannot be identified in these solutions, which indicates the necessity of introducing regularizations.

and CG iterations are shown in Fig. S3. The target cannot be identified from these reconstructions, which indicates the indispensable role of regularizations in this few-shot NLOS imaging scenario.

4. Reconstruction results of the pyramid

The three views of the reconstruction results of the pyramid are shown in Fig. S4. There are misleading artifacts in the top view and side view of the SOCR reconstruction, while the SSCR reconstruction does not contain background noise. For the F-K, LCT and D-LCT methods, we use the linear interpolation technique to pre-process the signal. We also use the zero-padding, nearest-neighbor, and makima(the modified Akima piecewise cubic Hermite in-
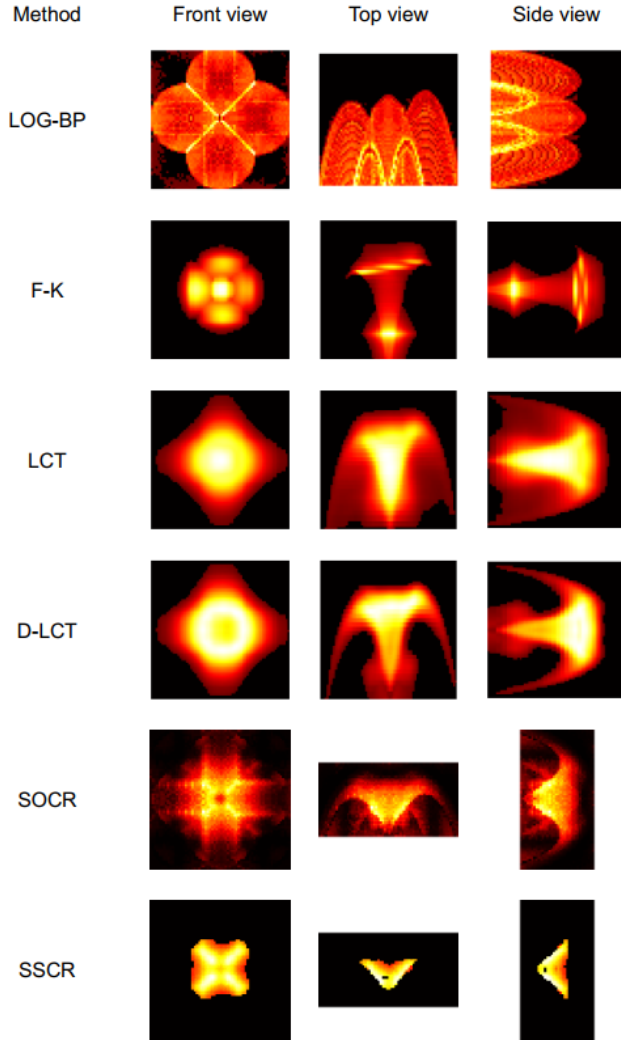
Figure S4. The three views of the pyramid reconstructed with 3×3 confocal synthetic signal.

terpolation, provided by the Matlab software) interpolation techniques to pre-process the signal. The F-K, LCT and D-LCT reconstructions with these signals are shown in Fig. S5, Fig. S6, and Fig. S7, respectively. The shape of the target cannot be correctly reconstructed with these methods.

5. Reconstruction results of the statue

In real-world applications, the measured signal is heavily corrupted with noise. As shown in Fig. S8, the LOG-BP reconstructions of the statue are noisy in few-shot NLOS imaging scenarios and the target cannot be identified. Reconstructions of the F-K, LCT and D-LCT methods with different number of illumination points and signal pre-processing techniques are shown in Fig. S9 to Fig. S23. See also Fig. 6 in the main article for a comparison with the proposed method.
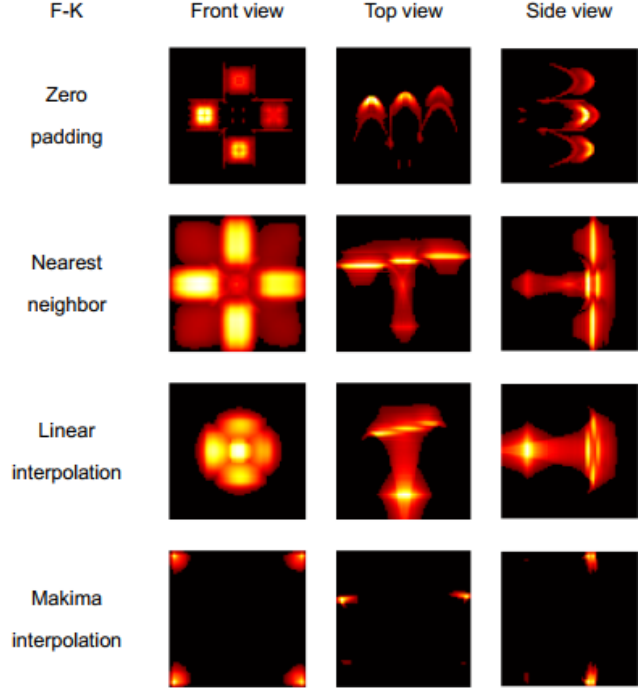
Figure S5. The F-K reconstructions of the pyramid with signal pre-processed by different interpolation techniques.
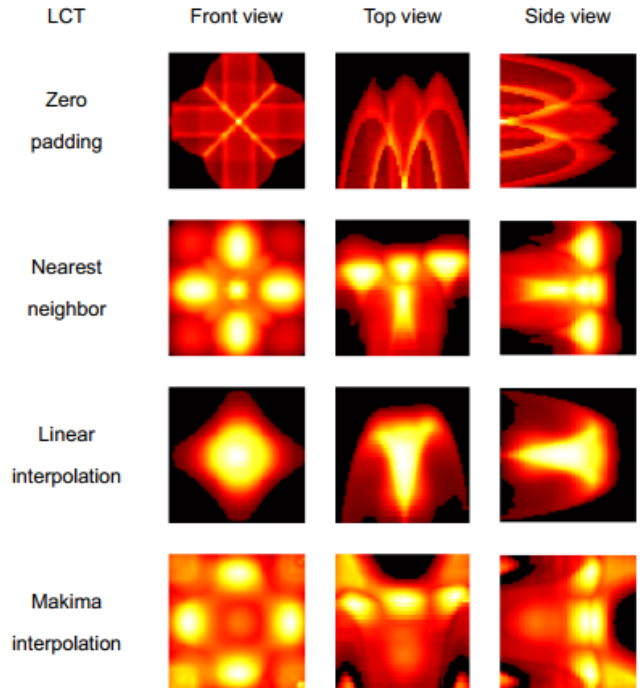
Figure S6. The LCT reconstructions of the pyramid with signal pre-processed by different interpolation techniques.

References

[1] Jian-Feng Cai, Hui Ji, Zuowei Shen, and Gui-Bo Ye. Data-driven tight frame construction and image denoising. *Applied*
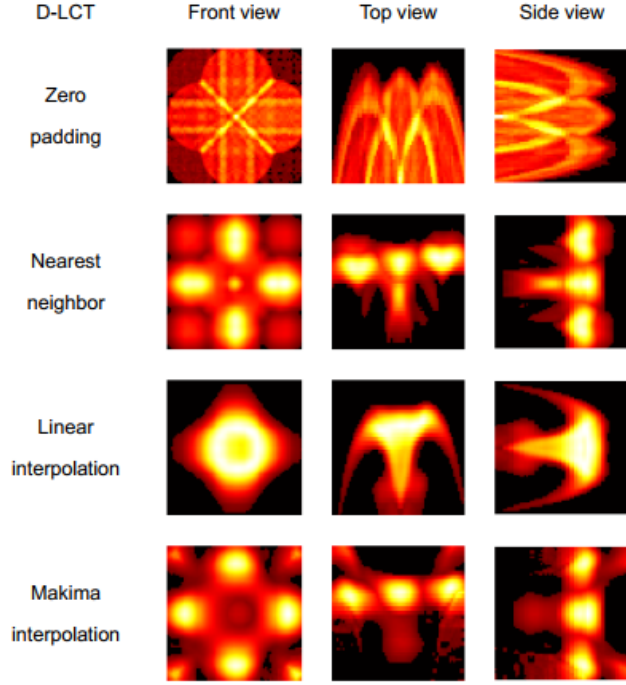
Figure S7. The D-LCT reconstructions of the pyramid with signal pre-processed by different interpolation techniques.
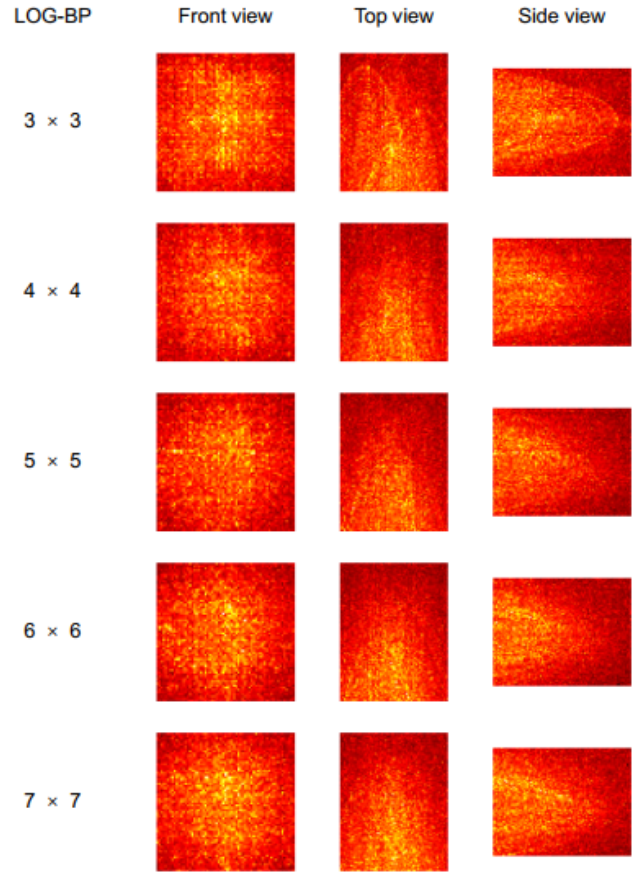
Figure S8. The LOG-BP reconstructions of the instance of the statue. See Fig. 6 in the main article for a comparison.

and Computational Harmonic Analysis, 37(1):89–105, 2014. 3

[2] Tom Goldstein and Stanley Osher. The split bregman method for l1-regularized problems. *SIAM Journal on Imaging Sciences*, 2(2):323–343, 2009. 2

[3] Martin Laurenzis and Andreas Velten. Feature selection and back-projection algorithms for non-line-of-sight laser-gated viewing. *Journal of Electronic Imaging*, 23(6):063003, 2014. 2

[4] David B. Lindell, Gordon Wetzstein, and Matthew O'Toole. Wave-based non-line-of-sight imaging using fast f-k migration. *ACM Trans. Graph. (SIGGRAPH)*, 38(4):116, 2019. 2, 4

[5] Xiaochun Liu, Sebastian Bauer, and Andreas Velten. Phasor field diffraction based reconstruction for fast non-line-of-sight imaging systems. *Nature Communications*, 11(1):1645, Apr 2020. 2

[6] Xintong Liu, Jianyu Wang, Zhupeng Li, Zuoqiang Shi, Xing Fu, and Lingyun Qiu. Non-line-of-sight reconstruction with signal–object collaborative regularization. *Light: Science & Applications*, 10(1):198, Sep 2021. 2, 3, 4

[7] Xintong Liu, Jianyu Wang, Leping Xiao, Zuoqiang Shi, Xing Fu, and Lingyun Qiu. Non-line-of-sight imaging with arbitrary illumination and detection pattern. *arXiv preprint arXiv:2211.00648*, 2022. 3

[8] Matthew O'Toole, David B. Lindell, and Gordon Wetzstein. Confocal non-line-of-sight imaging based on the light-cone transform. *Nature*, 555(7696):338–341, Mar 2018. 2

[9] Sean I. Young, David B. Lindell, Bernd Girod, David Taubman, and Gordon Wetzstein. Non-line-of-sight surface reconstruction using the directional light-cone transform. In *Proceedings of the IEEE/CVF Conference on Computer Vision and Pattern Recognition (CVPR)*, June 2020. 2
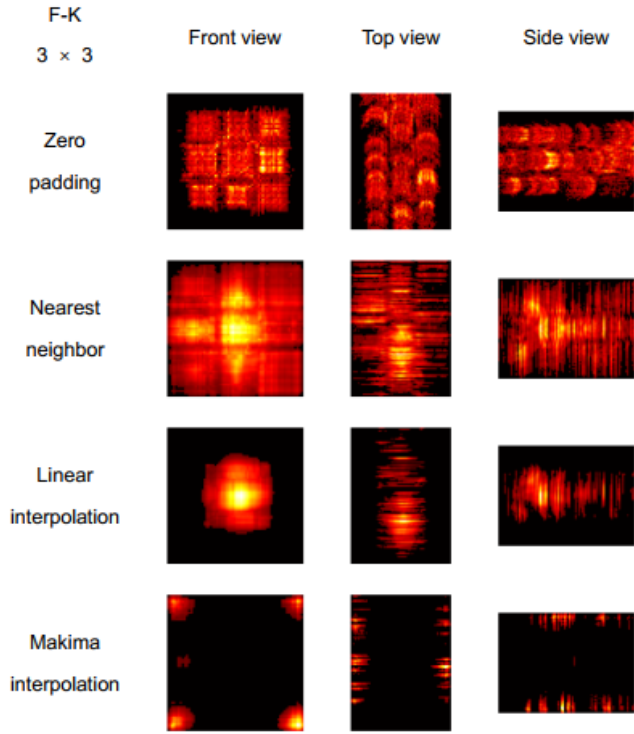
Figure S9. The F-K reconstructions of the statue using 3×3 confocal signal and different signal interpolation techniques.
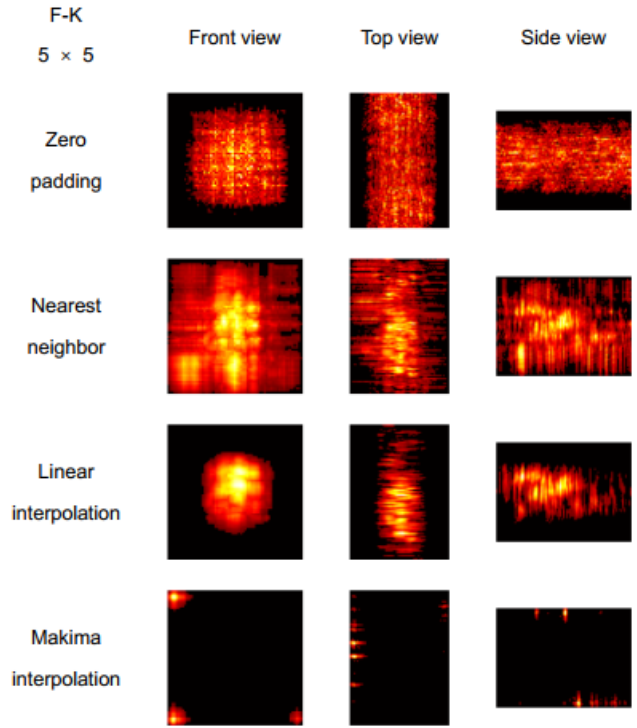

Figure S11. The F-K reconstructions of the statue using 5×5 confocal signal and different signal interpolation techniques..
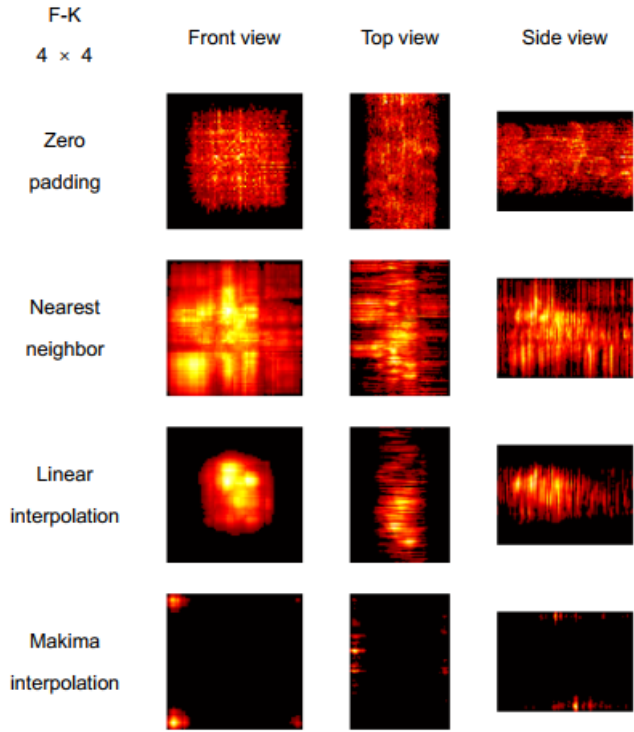

Figure S10. The F-K reconstructions of the statue using 4×4 confocal signal and different signal interpolation techniques.
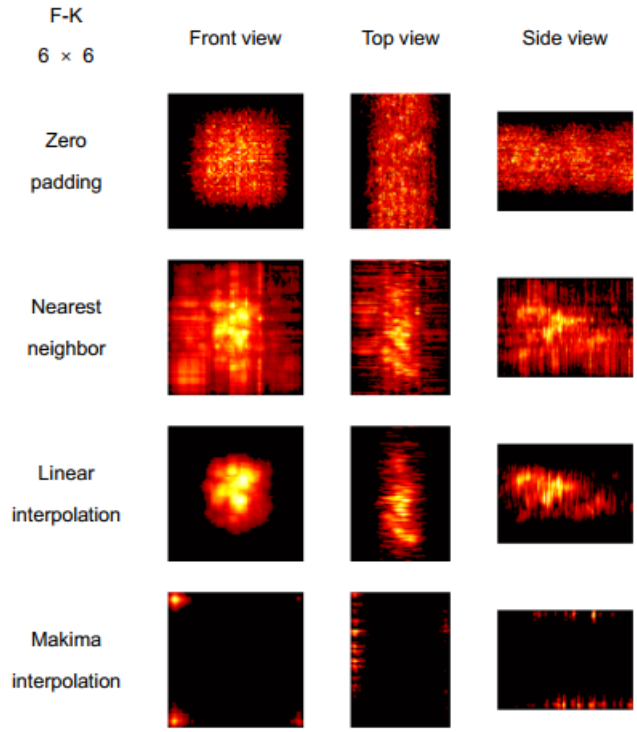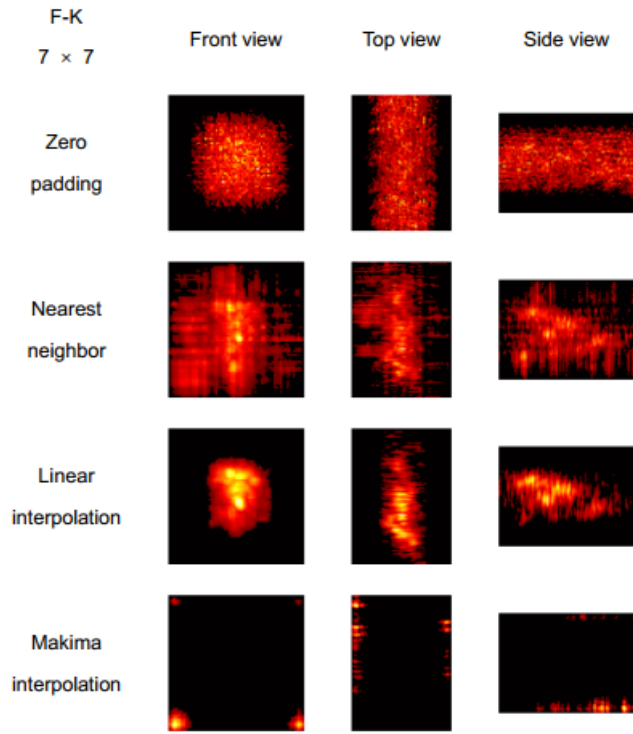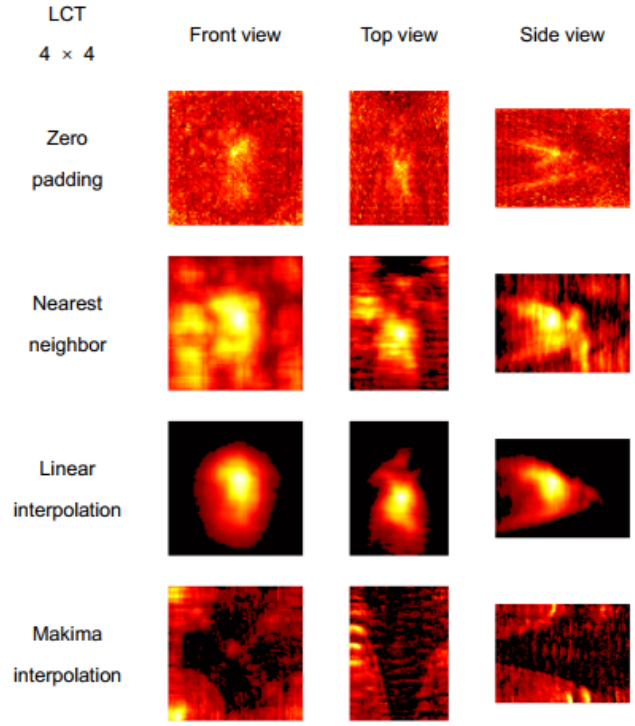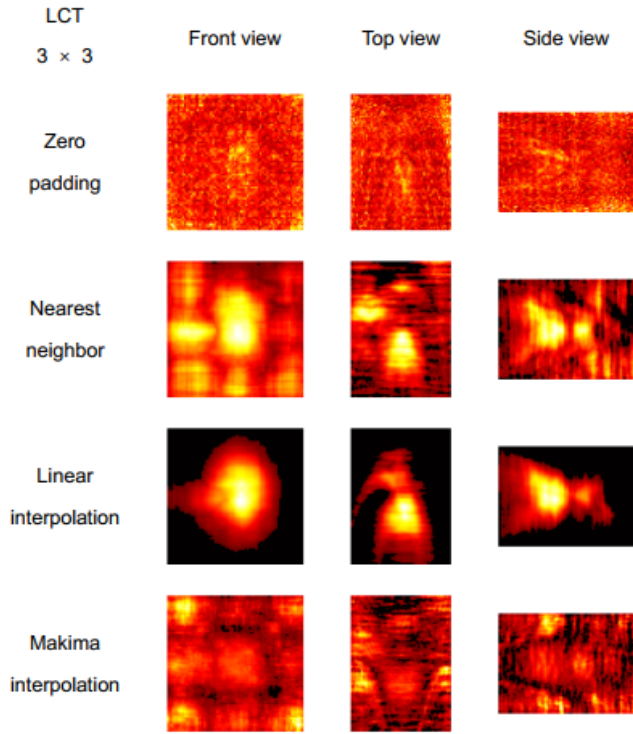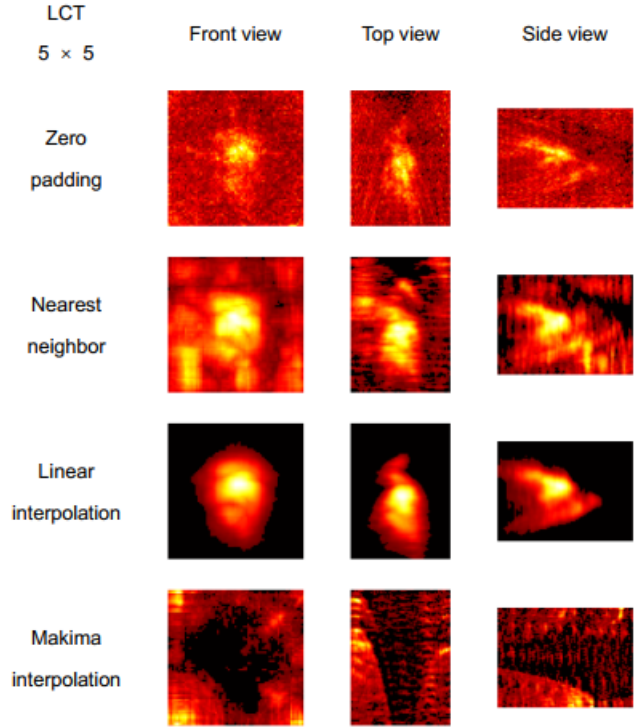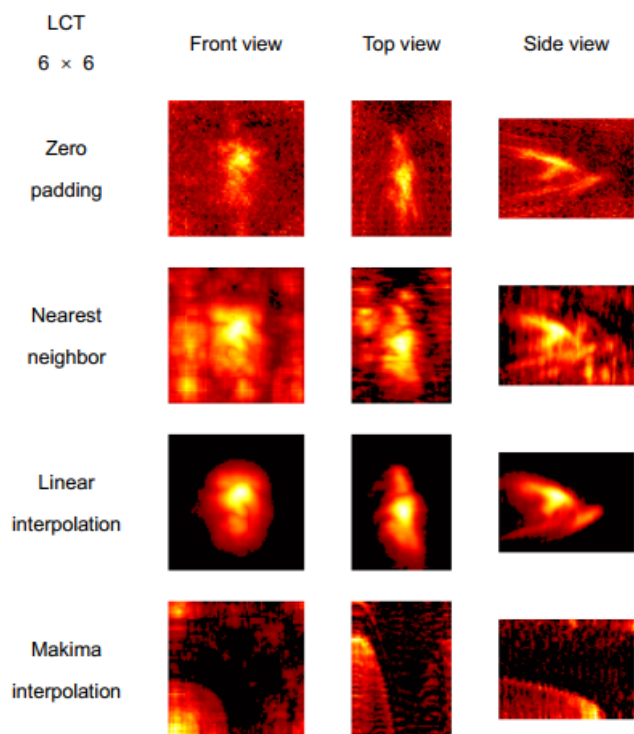

Figure S12. The F-K reconstructions of the statue using 6×6 confocal signal and different signal interpolation techniques.
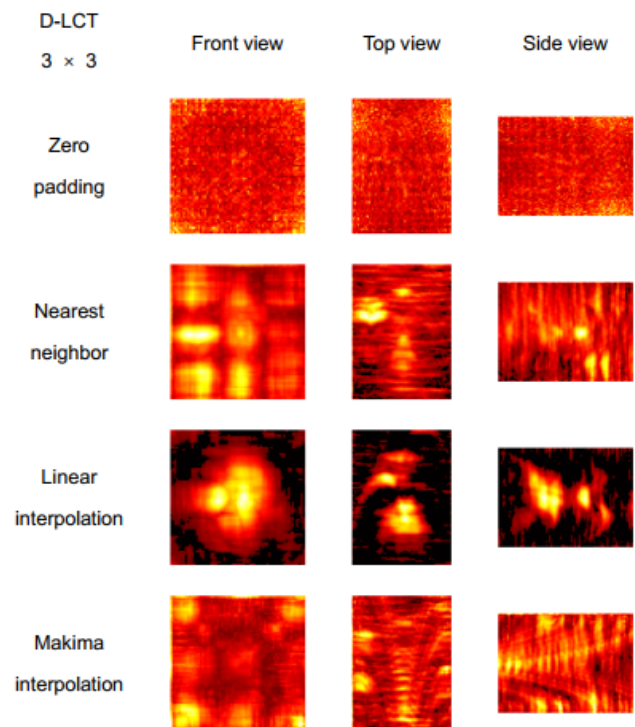
Figure S13. The F-K reconstructions of the statue using 7×7 confocal signal and different signal interpolation techniques.

Figure S15. The LCT reconstructions of the statue using 4×4 confocal signal and different signal interpolation techniques.

Figure S14. The LCT reconstructions of the statue using 3×3 confocal signal and different signal interpolation techniques.
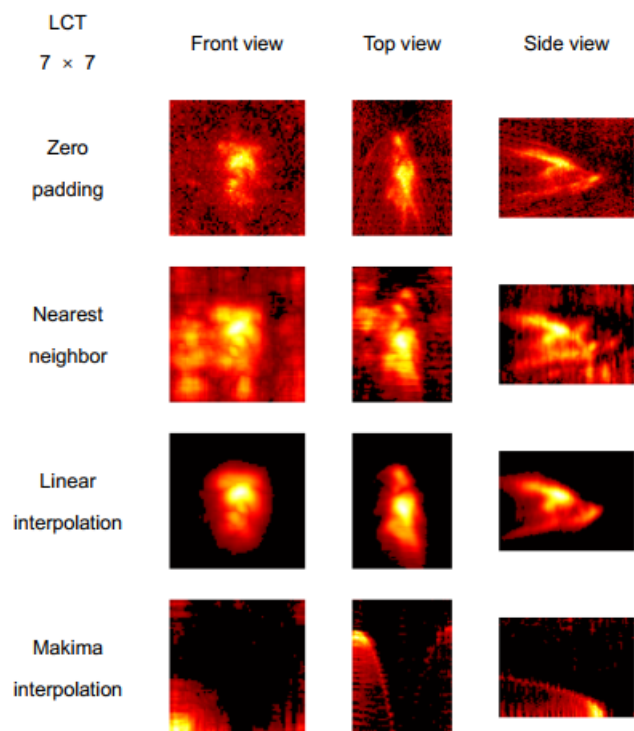

Figure S16. The LCT reconstructions of the statue using 5×5 confocal signal and different signal interpolation techniques.
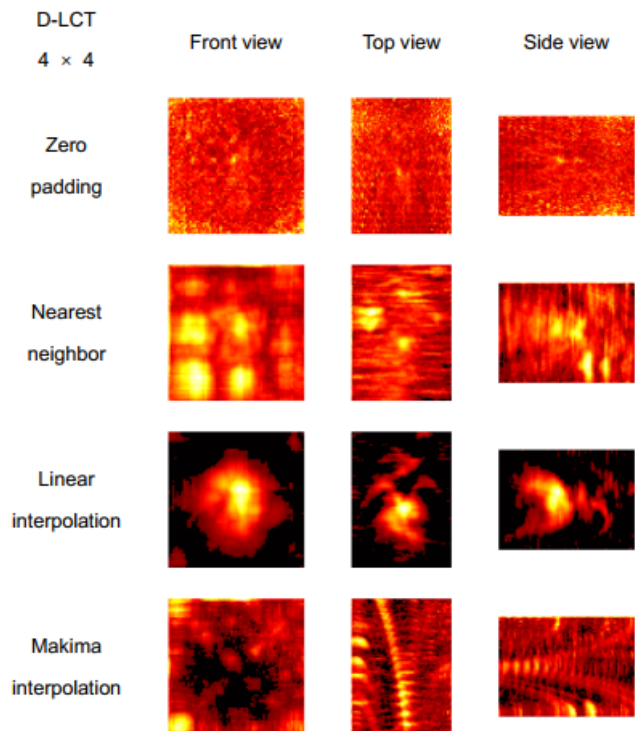
Figure S17. The LCT reconstructions of the statue using 6×6 confocal signal and different signal interpolation techniques.

Figure S19. The D-LCT reconstructions of the statue using 3×3 confocal signal and different signal interpolation techniques.
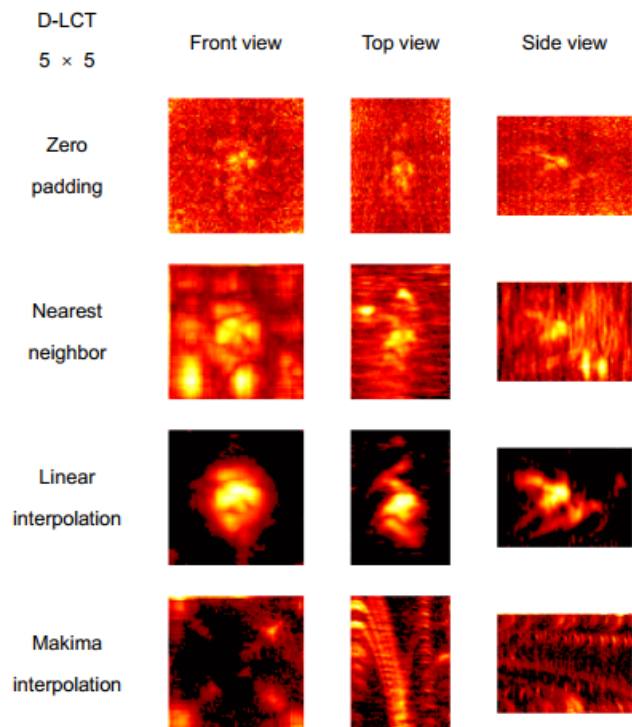

Figure S18. The LCT reconstructions of the statue using 7×7 confocal signal and different signal interpolation techniques.

Figure S20. The D-LCT reconstructions of the statue using 4×4 confocal signal and different signal interpolation techniques.

Figure S21. The D-LCT reconstructions of the statue using 5×5 confocal signal and different signal interpolation techniques.
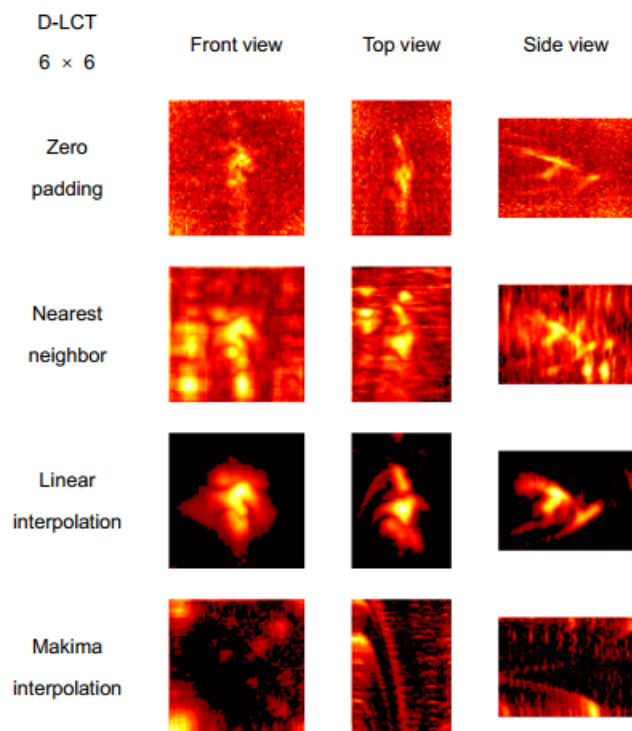

Figure S22. The D-LCT reconstructions of the statue using 6×6 confocal signal and different signal interpolation techniques.
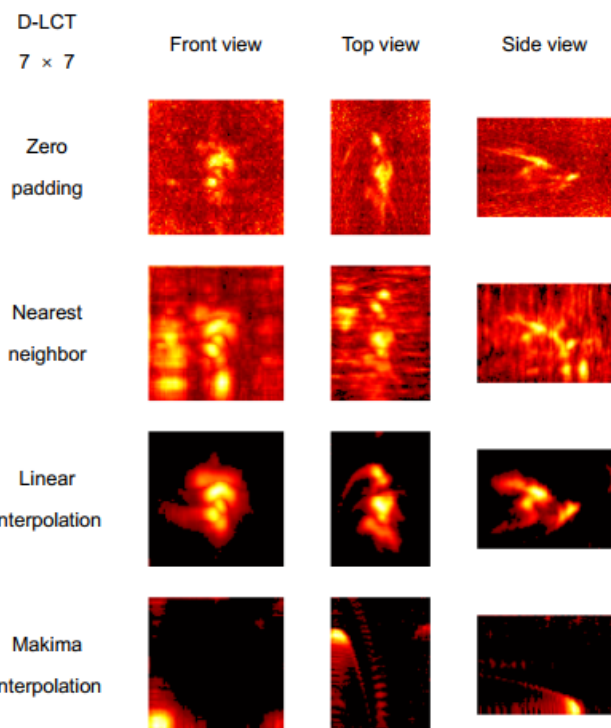

Figure S23. The D-LCT reconstructions of the statue using 7×7 confocal signal and different signal interpolation techniques.